
Science
Advances
19 APRIL 2024
AAAS

APPLIED PHYSICS

Acoustothermal transfection for cell therapy

Xiufang Liu[1]†, Ning Rong[1]†, Zhenhua Tian[2], Joseph Rich[3], Lili Niu[1], Pengqi Li[1], Laixin Huang[1], Yankai Dong[4], Wei Zhou[1], Pengfei Zhang[5], Yizhao Chen[5], Congzhi Wang[6], Long Meng[1]*, Tony Jun Huang[7]*, Hairong Zheng[1]*

Transfected stem cells and T cells are promising in personalized cell therapy and immunotherapy against various diseases. However, existing transfection techniques face a fundamental trade-off between transfection efficiency and cell viability; achieving both simultaneously remains a substantial challenge. This study presents an acoustothermal transfection method that leverages acoustic and thermal effects on cells to enhance the permeability of both the cell membrane and nuclear envelope to achieve safe, efficient, and high-throughput transfection of primary T cells and stem cells. With this method, two types of plasmids were simultaneously delivered into the nuclei of mesenchymal stem cells (MSCs) with efficiencies of 89.6 ± 1.2%. CXCR4-transfected MSCs could efficiently target cerebral ischemia sites in vivo and reduce the infarct volume in mice. Our acoustothermal transfection method addresses a key bottleneck in balancing the transfection efficiency and cell viability, which can become a powerful tool in the future for cellular and gene therapies.

INTRODUCTION

Gene and cell therapies are emerging as promising therapeutic strategies to treat various diseases such as cancer (*1*, *2*), genetic disorders (*2*, *3*), cardiovascular diseases (*4*, *5*), and ischemic stroke (*6*, *7*). Because of the success of therapeutic strategies based on CRISPR-Cas9 gene editing (*5*, *8*–*10*), there is an increasing need to deliver large plasmids into cells in a high-throughput, efficient, and biocompatible manner. Primary T cells and stem cells often have robust intracellular defense mechanisms that restrict the entry of foreign DNA or RNA into nuclei. Cytosolic nucleases and other cellular processes can degrade or eliminate the plasmid DNA (pDNA) in the cytoplasm, resulting in low transfection efficiency (*11*, *12*). The use of large plasmids makes it possible to regulate complex and multiple genes, as well as their expression, concurrently, which can be important for achieving the desired therapeutic effects. For example, plasmid-based CRISPR-Cas9 gene editing (*5*, *8*, *9*, *13*) or constitutive androstane receptor (CAR)–T therapy (*14*, *15*) needs to deliver large pDNA to enhance tissue-specific targeting or therapeutic effects. However, for therapeutic cells such as primary T cells and primary stem cells, the conventional techniques based on viral vectors (*16*, *17*), cationic lipids (*16*–*18*), or electroporation (*17*, *19*) suffer from low delivery efficiencies (*20*, *21*), and it is difficult to deliver large nucleic acid to these types of cells (*22*, *23*). Moreover, T cells and stem cells are delicate and sensitive to external stimulation. Viral-based transfection may trigger an immune response, affecting their viability and functionality (*11*, *12*). In addition, electroporation usually requires specific high-conductivity buffers and strong electric fields that may cause irreversible side effects on the genes and cells, including gene alteration that decreases the immune function (*20*), severe cell damage, or even cell death (*24*). Furthermore, electroporation requires cell-specific and plasmid-specific optimization, leading to requirements for highly trained personnel and limited adaptability of protocols between applications. As a result, intense research efforts have focused on the development of alternative transfection approaches, which can meet the demands of the rapidly evolving field of cell and gene therapy.

With the advancement of micro/nano technologies, vector-free transfection techniques based on nanostructures (*21*, *25*–*28*) and microfluidic cell squeezing (*16*, *20*, *29*, *30*) have been introduced in recent years. They apply mechanical forces on cells to transiently enhance the permeabilities of both the cellular membrane and nuclear envelope to allow foreign cargo into the cytoplasm and nucleus. Although the methods based on nanostructures, such as nanoneedles (*16*, *25*, *31*) and nanostraws (*25*, *27*), can deliver large cargos into the nucleus with high efficiencies, it is very challenging to scale up these methods. On the other hand, microfluidic cell squeezing methods, which deform cells using fluid shearing (*32*–*34*) or microconstrictions (*26*, *35*, *36*), can realize efficient delivery of small cargos (<3000 kDa) into cells, but achieving efficient delivery of large plasmids is still a challenge (*20*, *29*, *37*, *38*). In addition, the methods based on nanostructures or microfluidic cell squeezing usually experience clogging issues and the device structures need to be redesigned for treating cells with different sizes.

In addition to the aforementioned techniques, the application of high-frequency acoustic waves (*39*–*42*) has proven to be an effective approach for achieving physical transfection through ultrasound-induced microbubbles (*43*–*46*) or through the direct application of acoustic forces to cells (*47*–*50*). Although bubble-based sonoporation techniques can reversibly open pores on cell membranes for intracellular delivery, they highly rely on the size, location, and concentration of the microbubbles (*51*, *52*). Furthermore, the rapid collapse of the microbubble generates a shock wave that may lead to irreversible damage to cells and genes (*53*). Therefore, the ultrasound community is actively looking for bubble-free ultrasonic transfection mechanisms (*54*–*56*). Unfortunately, previous bubble-free ultrasonic techniques suffer from low efficiencies (typically less than 20%) (*57*) for primary

[1]CAS Key Laboratory of Health Informatics, Shenzhen Institutes of Advanced Technology, Chinese Academy of Sciences, 1068 Xueyuan Avenue, Shenzhen 518055, China. [2]Department of Mechanical Engineering, Virginia Polytechnic Institute and State University, Blacksburg, VA 24061, USA. [3]Department of Biomedical Engineering, Duke University, Durham, NC 27708, USA. [4]School of Life Sciences, Tsinghua University, Beijing 100084, China. [5]Guangdong Key Laboratory of Nanomedicine, CAS-HK Joint Lab for Biomaterials, Shenzhen Institutes of Advanced Technology, Chinese Academy of Sciences, Guangdong 518055, China. [6]National Innovation Center for Advanced Medical Devices, 385 Mintang Road, Shenzhen 518131, China. [7]Thomas Lord Department of Mechanical Engineering and Materials Science, Duke University, Durham, NC 27708, USA.
*Corresponding author. Email: long.meng@siat.ac.cn (L.M.); tony.huang@duke.edu (T.J.H.); hr.zheng@siat.ac.cn (H.Z.)
†These authors contributed equally to this work.

cells. Low efficiencies and low post-transfection cell viabilities have limited the clinical utility of existing ultrasonic techniques, especially in autologous cell therapy applications where the number of donor cells is limited. Overall, ultrasonic transfection methods and other existing physical transfection techniques have yet to simultaneously achieve the following features critical for gene and cell therapies, including (i) fast and efficient transfection for delivering genes into the nuclei of hard-to-transfect cells such as primary T cells and stem cells, (ii) the simultaneous delivery of multiple types of large plasmids for expressing multiple gene products, and (iii) comprehensive demonstrations of the in vivo functionality of transfected cells.

This study presents a bubble-free acoustothermal transfection technique, which takes advantage of the combined acoustic and thermal effects induced by surface acoustic waves (SAWs) to enhance both the cell membrane and nuclear envelope transient permeabilities and enable safe, efficient, and high-throughput transfection of hard-to-transfect cells. Our technique not only applies acoustic forces on cells to perforate cells but also leverages thermal pulses induced by the viscous damping of acoustic waves to perforate the nuclear membrane more easily. Our experimental study shows that both the cell membrane and nuclear envelope permeabilities can be enhanced to deliver large functional cargos to the cytoplasm and nucleus in 5 min with a viability of 89.7 ± 0.8% for MCF-7 cells. Moreover, our technique is scalable, and multiple acoustothermal transfection units can be integrated. Nearly 1.7 million cells can be transfected in 1 min with 6 × 8 parallel units. We have validated our method by demonstrating its ability to efficiently deliver plasmids into the nuclei of hard-to-transfect cells, including mesenchymal stem cells (MSCs) and primary T cells. The transgene could be expressed at 14 hours after treatment with expression efficiencies of 89.0 ± 0.9% measured with fluorescence imaging and 82.6% measured by flow cytometry for delivering CXCR4 plasmids, and the efficiencies for delivering brain-derived neurotrophic factor (BDNF) plasmids were 90.3 ± 2.4% and 86.7%. With two types of plasmids, the gene expression efficiencies could reach 89.6 ± 1.2% (89.4% with flow cytometry) for MSCs at 24 h. For T cells, a single type of plasmid expression reached 85.0 ± 0.6% (81.3% with flow cytometry) in 24 hours. We showed that the transfected cells could realize therapeutic functionalities in vivo by injecting transfected MSCs into ischemic stroke mice models. With multiple key features including high efficiency (both in vitro and in vivo), high throughput, and high biocompatibility when quickly delivering large plasmids into hard-to-transfect cells, our acoustothermal transfection technique addresses the key limitations of previous transfection methods and shows great potential for both biomedical research and clinical applications such as immunotherapy and gene therapy.

RESULTS

Acoustothermal transfection for enhancing cell membrane and nuclear envelope permeabilities

Figure 1A shows a schematic of our developed acoustothermal transfection device with an array of 6 × 8 independent units (also see fig. S1 for a device photo). Each unit is composed of interdigital transducers (IDTs) plated on a $LiNbO_3$ substrate to generate standing SAWs, a polydimethylsiloxane (PDMS) well for hosting cells, and a 1-mm-thick PDMS layer covering the IDTs. When short-duration SAWs are generated by the IDTs, the PDMS layer delivers the generated acoustic energy to cells in the PDMS well. The PDMS layer also converts a portion of the acoustic energy to thermal energy, inducing temperature increases through its viscous damping.

For cells in our acoustothermal transfection device, they are subjected to SAW-induced stresses, acoustic streaming–induced shear forces, and short acoustothermal pulses, and their combination can effectively enhance the cell membrane and nuclear envelope permeabilities, thus enabling efficient transfection, as illustrated by the mechanism schematic in Fig. 1A. After the acoustothermal treatment, the transfected cells can be collected for down streaming research or therapeutic applications. For example, we have injected the transfected MSCs into a middle cerebral artery occlusion (MCAO) mouse through the vein tail for cell therapy and successfully demonstrated the therapeutic effect of MSCs transfected by our device.

To validate the membrane perforation capability enabled by our acoustothermal device, MCF-7 cells were stained with an impermeable nuclei acid staining dye propidium iodide (PI) and a live-cell identification reagent calcein acetoxymethyl ester (calcein-AM), which were used to indicate pore formation (red fluorescence) and cell viability (green fluorescence), respectively (*58*). After acoustothermal treatment enabled by exciting the IDT at 24 MHz, almost all the cells emitted red fluorescence, indicating a high perforation efficiency. Figure 1B shows the diffusion and accumulation of PI through all the intracellular space starting around the whole cell after the SAW exposure, which suggests a global cell membrane permeability enhancement and recovery occurring in minutes. The quantitative analysis result in Fig. 1C shows that the average red fluorescence intensity markedly increased during a 10-s SAW treatment (power, 1.2 W) and then remained nearly at a constant level.

To investigate the effect of acoustothermal transfection on the nuclear envelope integrity, we used the Cy5-tagged charged multivesicular body protein 4B (CHMP4B-Cy5), which is a major part of the endosomal sorting complex required for transport III complex that mediates membrane fusion for nuclear envelope repair (*59*). The CHMP4B typically exhibits a uniform distribution, while during the nuclear envelope repair process, it accumulates at the damage site of the nuclear envelope. After treatment, CHMP4B proteins were rapidly recruited to the nuclear envelope to generate transient foci (see Fig. 1D and fig. S2), indicating the nuclear envelope impairment. After 8 min, the number of CHMP4B foci on the nuclear envelope decreased to a lower level (Fig. 1E), suggesting that the nuclear envelope was repaired. This result demonstrates that the acoustothermal device can induce reversible nuclear envelope permeability change.

After the aforementioned tests on the membrane and nuclear envelope permeabilities, CdTe quantum dots (diameter, ~6.74 nm) delivery experiments were performed to investigate the capability of directly and quickly transporting nanocargos to cell nuclei. At 5 min after treatment, MCF-7 cells and their nucleus showed strong CdTe quantum dot fluorescence (Fig. 1F). Moreover, with the increase of time, more cells showed CdTe quantum dot fluorescence, and the quantum dot intracellular accumulation images at other time points was shown in fig. S3. The statistical result showed that the fluorescence intensity in the nucleus increased to a peak at 10 min after treatment (Fig. 1G). In addition to delivering small quantum dots, our acoustothermal device could deliver large nanocargos into the nucleus, as demonstrated by the successful delivery of carbon nanoparticles (diameter, ~43.5 nm) into MCF-7 cells within 5 min (fig. S4).

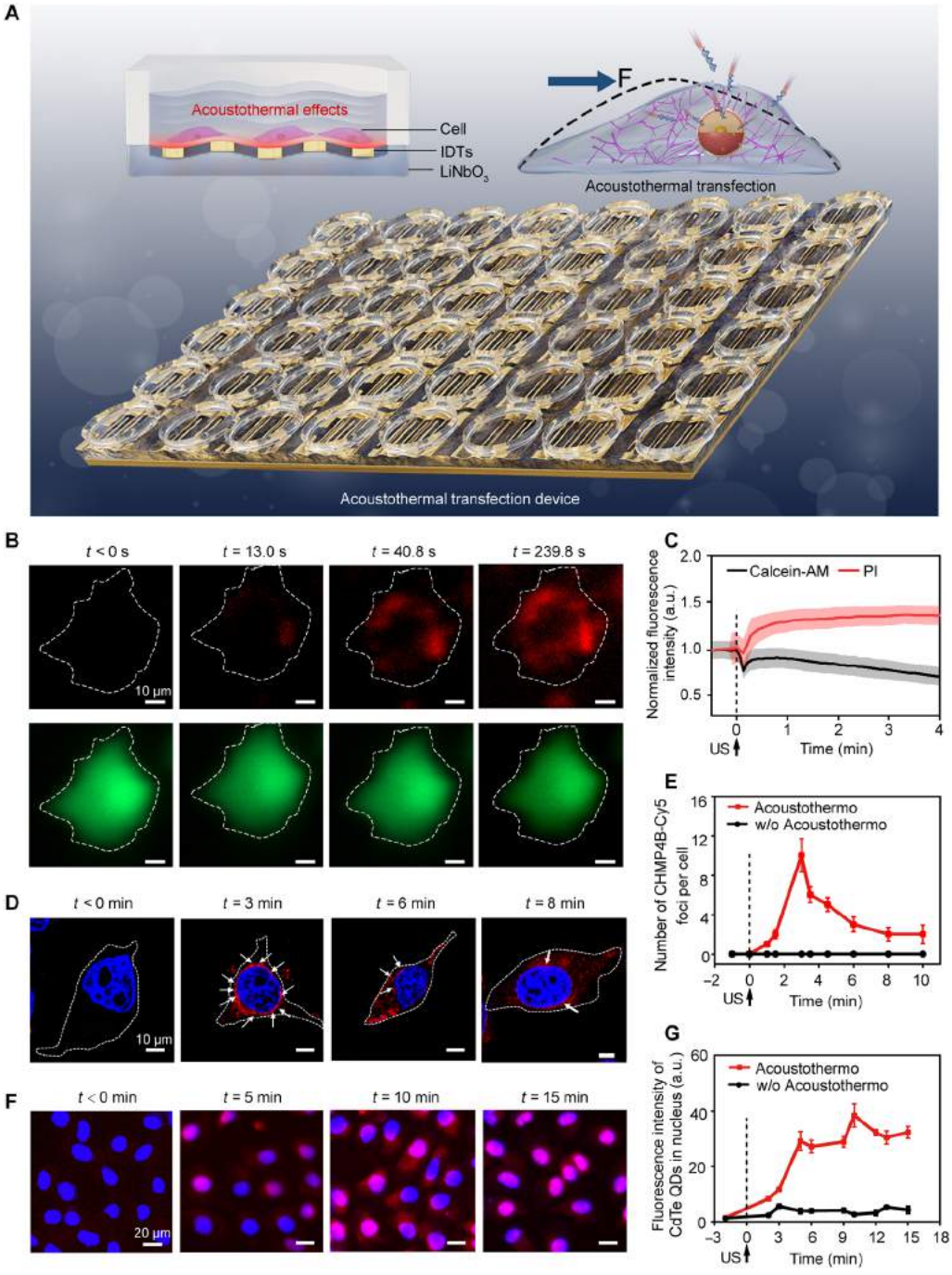

Fig. 1. Acoustothermal transfection for enhancing cell membrane and nuclear envelope permeabilities. (**A**) Schematics for illustrating the mechanism of acoustothermal transfection showing our developed acoustothermal transfection device with 6 × 8 units for high-throughput transfection. Each unit consists of IDTs for generating SAWs, a PDMS well for hosting cells, and a 1-mm-thick PDMS layer on top of the IDTs for delivering acoustic energy to cells and enabling local temperature increases through viscous damping. The combination of SAW-induced acoustic and thermal effects can enhance the transient permeabilities of the cell membrane and nuclear envelope to achieve efficient transfection of hard-to-transfect cells. (**B**) Time-sequential fluorescence images showing the cell membrane permeability change induced by 10 s of acoustothermal treatment. Propidium iodide (PI; red) and calcein-AM (green) are for characterizing the cell permeability changes and live MCF-7 cells. (**C**) Time history plots of mean PI and calcein-AM fluorescence intensities were obtained by extracting the intensities from fluorescence images in (B). Twenty cells' intensity changes were analyzed. The fluorescence intensity was normalized by the control group without acoustothermal treatment. a.u., arbitrary units. (**D**) Fluorescence images of CHMP4B-Cy5 foci (red) for validating the nuclear envelope permeability changes induced by 10 s of acoustothermal transfection. (**E**) The number of CHMP4B-Cy5 foci per cell for characterizing nuclear envelope rupture and resealing over time. Fluorescence areas larger than 5 μm^2 with a gray level higher than 30 were counted as CHMP4B-Cy5 foci. Ten cells were counted for the CHMP4B foci statistical analysis. (**F**) Confocal microscopy images showing acoustothermal transfection enabled the delivery of CdTe quantum dots (red) into nuclei. (**G**) Fluorescence intensity changes over time for characterizing the accumulation of CdTe quantum dots in nuclei [blue: 4′,6-diamidino-2-phenylindole (DAPI)]. Ten cells' intensity changes were presented. For all the statistical analysis, the experiment was repeated at least three times.

Biophysical mechanisms of acoustothermal transfection

For mechanism investigation, a laser Doppler vibrometer was used to measure the out-of-plane displacement field on a PDMS layer covering an IDT of our acoustothermal transfection device. The experimental results (Fig. 2A and movie S1) show strong SAWs generated on the top surface of the PDMS layer. The simulation results further revealed the distribution of acoustic pressure and the velocity field of acoustic streaming (fig. S5). We also performed experiments to characterize the acoustic wave–induced particle distributions in a PDMS well of our acoustothermal transfection device. The result showed that 5-μm polystyrene particles at the bottom of the PDMS well were moved to pressure node lines to construct a parallel line–like pattern, proving the generation of standing acoustic waves (Fig. 2B and movie S2). On the other hand, 2-μm polystyrene particles suspended in the PDMS well were subject to vortex-like acoustic streaming (Fig. 2C and movie S3). In addition, to determine whether cavitation was induced by the acoustothermal transfection device, we measured the frequency spectrum during SAW generation by using a laser Doppler vibrometer–based cavitation detection method. Previously, researchers found that stable and inertial cavitation could lead to harmonic and wide band acoustic noises (*46*). However, our acquired spectrum (Fig. 2D) shows one strong peak at the SAW frequency without harmonic frequencies or wide band noises. This observation indicates that our acoustothermal transfection method is free of stable and inertial cavitation. In addition to the acoustic effect on cells, we also observed that cells were exposed to short thermal pulses, as a portion of acoustic energy converted to thermal energy due to PDMS's viscous damping. A thermal imager was used to monitor the temperature changes of the top surface of the PDMS layer. The results show that the average temperature in 10 s of SAW treatment was 42°C (fig. S6).

As proven by the above characterization results, our acoustothermal transfection device can generate acoustic waves, induce temperature increases, and is free of cavitation. To optimize the treatment parameters of our acoustothermal device, we performed a parametric study with MCF-7 cells. As shown in the statistical results, the perforation efficiency (Fig. 2E) increased with the input power increase (from 0.2 to 1.2 W) and treatment time increase (from 5 to 20 s), and acoustothermal treatment with durations less than 10 s led to small viability reductions, as indicated by the CCK-8 assay results (Fig. 2F). On the basis of these results, the optimized treatment parameters (1.2 W and 10 s) were found. On the other hand, we performed comparison experiments to investigate sole acoustic, sole thermal (*16*), and their combined effects on membrane perforation efficiencies. The sole acoustic treatment was performed by using standing SAWs generated in a temperature-controlled area between two IDTs. The acquired fluorescence images (fig. S7) and statistical results (Fig. 2G) revealed that less than 5% MCF-7 cells showed PI fluorescence in groups with 10 s of sole thermal or acoustic treatment. When increasing the input power by 2.7 times and extending

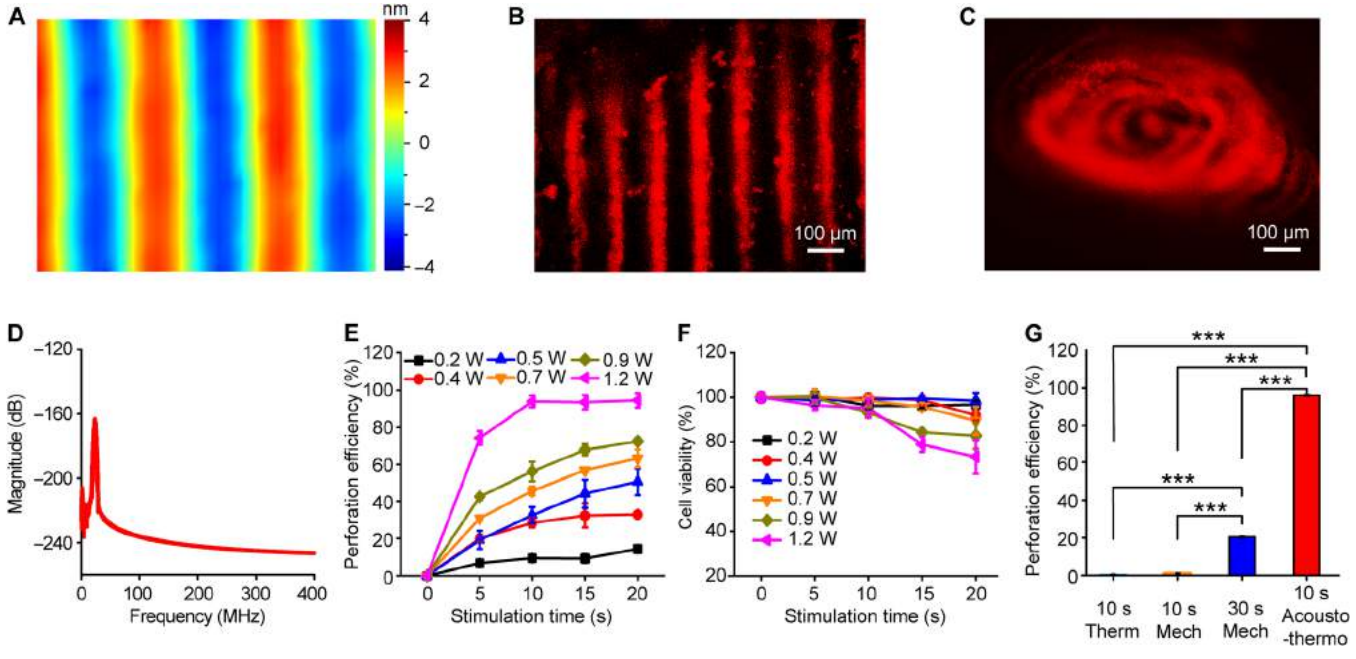

Fig. 2. Mechanism of acoustothermal transfection. (**A**) An out-of-plane displacement field of generated SAWs characterized by a laser Doppler vibrometer at the power of 1.2 W. (**B**) A fluorescence image showing 5-μm polystyrene particles at the bottom of a PDMS well can be arranged by SAW-induced acoustic radiation forces to form a parallel line–like distribution at the power of 1.2 W with continuous acoustic stimulus. (**C**) A fluorescence image showing 2-μm polystyrene particles suspended in a solution in a PDMS well are subjected to vortex-like acoustic streaming at the power of 1.2 W with continuous acoustic stimulus. (**D**) Frequency spectrum measured by a laser Doppler vibrometer during SAW generation. The spectrum shows a strong peak at the excitation frequency of 24 MHz without higher harmonics or wide band noises, indicating that our device is free of cavitation. (**E**) MCF-7 cell membrane perforation efficiencies characterized by using calcein-AM and PI fluorescence (cells with green fluorescence characterizing living cells and cells with green and red fluorescence characterizing perforated cells). (**F**) MCF-7 cell viability data measured using CCK-8 assays. (**G**) Cell membrane perforation efficiencies were achieved by different methods, including 10 s of sole thermal treatment (10 s Therm), 10 s of sole acoustic mechanical treatment (10 s Mech), 30 s of sole acoustic mechanical treatment (30 s Mech), and 10 s of treatment with our acoustothermal transfection device (10 s Acoustothermo) that leverages both the acoustic and thermal effects. MCF-7 cells were applied to estimate the perforation effect.

the treatment time to 30 s for a sole acoustic case, the perforation efficiency was increased to 20.5 ± 0.7%. In contrast, for the group with 10 s of acoustothermal transfection, ~96% cells showed PI fluorescence, demonstrating a significant enhancement of the perforation efficiency. Moreover, the sonoporation efficiency showed a nearly uniform distribution within the whole chamber (fig. S8). These results prove the advantage of combining acoustic and thermal effects for substantial enhancement of cell perforation efficiency.

Transfection of MCF-7, MSCs, and CD3$^+$ T cells

To investigate the plasmid delivering capability of acoustothermal transfection, we performed a series of experiments using MCF-7 cells and hard-to-transfect cells (MSCs and primary CD3$^+$ T cells) and compared our acoustothermal method to lipofection and electroporation. We compared our acoustothermal method (with optimized power 1.2 W and treatment time 10 s) to lipofection (Lipo 2000, Life Technologies) by delivering lentivirus vector plasmid (FUGW) carrying green fluorescent protein [GFP; 9951 bp, 6.5 MDa, denoted as PUGW–enhanced GFP (EGFP)] into MCF-7 cells. Figure S9A shows the acquired fluorescence images for both methods and fig. S9 (B and C) compares their quantitative results, including GFP expression efficiencies and fluorescence intensities at 12 hours after treatment. At 12 hours, MCF-7 cells treated by our acoustothermal device showed strong green fluorescence with an efficiency of 96.1 ± 0.5%. Consistent with the sonoporation outcome, the DNA expression also showed a nearly uniform distribution across the whole well (fig. S10). In contrast, cells in the Lipo 2000 group showed green fluorescence at 12 hours with an efficiency of 79.7 ± 2.2%.

The ability to deliver CXCR4-EGFP (7107 bp, 4.6 MDa) and BDNF (BDNF-mCherry, 6859 bp, 4.5 MDa) plasmids into MSCs was tested. At 14 hours after acoustothermal transfection, MSCs delivered with CXCR4-EGFP plasmids showed strong green fluorescence with gene expression efficiencies of 89.0 ± 0.9% (based on the fluorescence imaging data in Fig. 3C) and 82.6% (based on flow cytometry data in fig. S11), while cells treated by electroporation showed fluorescence at 24 hours, indicating that the acoustothermal transfection allowed for more efficient gene delivery. After 24 hours, high efficiency was maintained (~86.4%, based on the flow cytometry data in Fig. 3B), while the electroporation group's efficiency was less than 20%. For delivering BDNF-mCherry plasmids into MSCs using acoustothermal transfection, efficient gene expression in 14 hours was achieved (Fig. 3, D and F, and fig. S12). We found the acoustothermal transfection could simultaneously deliver different plasmids, for example, equally mixed CXCR4-EGFP and BDNF-mCherry plasmids. At 14 hours after acoustothermal transfection, MSCs successfully expressed both CXCR4 and BDNF proteins with a dual plasmid expression efficiency of 88.2 ± 2.1% (based on the fluorescence images in Fig. 3, G and I), which further reached 89.6 ± 1.2% at 24 hours (based on the fluorescence images in Fig. 3G). MSCs in the acoustothermal treatment group exhibited higher gene expression efficiencies and higher fluorescence intensities compared to the cells treated by lipofection and electroporation (fig. S14, A to C).

We further demonstrated the capability of our acoustothermal transfection for efficiently delivering plasmids into primary T cells, which are considered one of the hardest-to-transfect primary cells. Cy3-labeld DNA could realize fast intracellular uptake even in the nuclei in 30 min (fig. S15). For the control group treated by electroporation, the efficiency of delivering EGFP plasmids (4731 bp, 3 MDa) into CD3$^+$ T cells was very low, approximately 12.1 ± 1.6% with fluorescence images at 24 hours after treatment (Fig. 3L). In contrast, in the acoustothermal transfection group, EGFP expression efficiencies of CD3$^+$ T cells at 14 hours were 80.8 ± 3.1% (based on the fluorescence images in Fig. 3L) and 78.6% (based on the flow cytometry data in fig. S16), and these efficiencies further increased to 85.0 ± 0.6% (Fig. 3L) and 81.3% (Fig. 3K) at 24 hours. Higher EGFP fluorescence intensities were also observed (fig. S14D).

Biocompatibility at the genetic and cellular levels

RNA sequencing experiments were performed to analyze possible side effects of acoustothermal transfection at the gene level. Compared to a control group free of acoustothermal transfection, the differential expression analysis identified no differentially expressed genes from the acoustothermal transfection group at 24 hours after treatment (Fig. 4A). The gene set enrichment analysis (GSEA) was performed as well. The nominal P value, the false discovery rates (FDR) calculated with the Benjamini-Hochberg method, and the normalized enrichment score (NES) were assigned to indicate the gene set enrichment. Typically, the GSEA results indicate significant gene mutation, if $P < 0.05$, FDR < 0.25, and NES > 1. Our results (Fig. 4B with $P = 0.36$, FDR = 0.6, and NES = 1.02) indicate that acoustothermal transfection had a minimal impact on gene mutation. In addition, long-term cell viability after acoustothermal transfection was characterized using multiple methods, including fluorescence imaging, flow cytometry, and CCK-8 assays. Our results showed that more than 95% of cells maintained their viability at various time points (Fig. 4, C and D, and figs. S17 to S19). In Fig. 4E, the acoustothermal transfection treatment group showed significant cell number increasing over time similar to the control group, indicating the cells kept their proliferative ability after acoustothermal treatment. The aforementioned gene damage, gene mutation, cell viability, and cell proliferation characterization results indicate that acoustothermal transfection supports high biocompatibility for long-term cell growth. Furthermore, about 90% of MSCs (Fig. 4F) and CD3$^+$ T cells (Fig. 4G) could maintain their viability at 24 hours after the SAW exposure at 1.2 W with a duration of 10 s. Higher input power or longer stimulation time may cause a marked drop in viability. For the sole thermal stimulation experiment, temperature was held at 51.2°C for 10 min in a water bath, which did not induce obvious cell death in MSCs (fig. S20A) or in CD3$^+$ T cells (fig. S20B). Obvious cell death was found at a higher temperature, such as 62.9°C. The excitation time and the maximum spatial-average temperature applied in the transfection experiment was 10 s and 51.2°C, which was much shorter exposure time to similar viable temperatures. The long-time viability assay further confirmed the acoustothermal transfection treatment technique has a high biocompatibility.

Further experiments were carried out to investigate the viability of transfected cells in the presence of plasmids using flow cytometry. The flow cytometry results indicate that the viability of MCF-7 cells, 24 hours after acoustothermal treatment without the participation of pDNA plasmids, was 90.9% (Fig. 4H). Upon adding pDNA plasmids and co-incubating with the cells, a slight reduction in MCF-7 cell viability was observed, approximately 85.9%. This minor decrease may be attributed to the DNA toxicity of the plasmids. Consistent with the MCF cell results, both MSC cells and CD3$^+$ T cells exhibited a declining trend in viability in the presence of plasmids. The viability of MSC cells and CD3$^+$ T cells was 83.9 and 84.4%, respectively (Fig. 4, I and J).

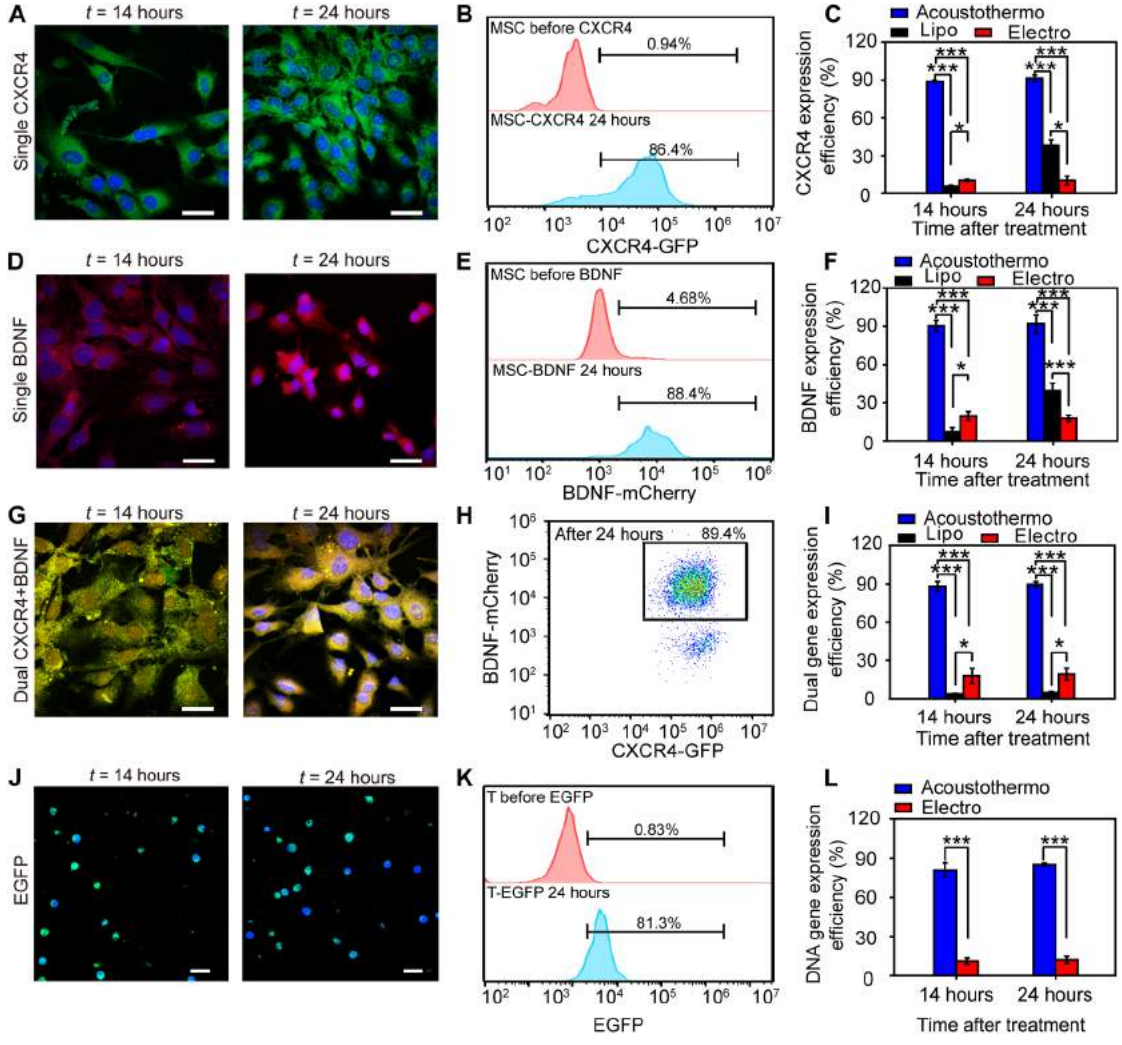

Fig. 3. Results for the acoustothermal transfection of MSCs and CD3$^+$ T cells. (**A**) Fluorescence images (blue, DAPI; green, CXCR4) and quantitative characterization results (post-treatment CXCR4 expression efficiency) for the transfection of CXCR4 plasmids into MSCs with (**B**) flow cytometry and (**C**) fluorescence images. (**D**) Fluorescence images (blue, DAPI; red, BDNF) and quantitative characterization results (post-treatment BDNF expression efficiency) for the transfection of BDNF plasmids into MSCs with (**E**) flow cytometry and (**F**) fluorescence images. The expression efficiency of CXCR4 (or BDNF) at 14 hours after treatment is 89.0% (or 90.3%), which is much higher than the efficiency of the Lonza electroporation group. (**G**) Results for the simultaneous transfection of dual types of plasmids (CXCR4-EGFP and BDNF-mCherry). (**H**) Transfection efficiency of the simultaneous transfection of dual types of plasmids (CXCR4-EGFP and BDNF-mCherry) with flow cytometry. (**I**) Compared to the Lonza electroporation method, which is difficult to achieve dual transfection, our acoustothermal transfection method can achieve high efficiency (88.2%) of expressing dual types of genes at 14 hours after treatment. The dual gene expression efficiency further increases to 89.4% at 24 hours after treatment. (**J**) Fluorescence images (blue, DAPI; green, EGFP) and quantitative characterization results (post treatment gene expression efficiency) for the transfection of EGFP plasmids into CD3$^+$ T cells with (**K**) flow cytometry and (**L**) fluorescence images. Compared to the Lonza electroporation method, the acoustothermal transfection method can achieve a high transfection efficiency of 81.3% at 24 hours after treatment. $^{**}P < 0.01$ and $^{***}P < 0.001$. For all the statistical analysis, three repeated experiments were conducted.

In vivo validation with a stroke model

For cell or gene therapy, the transfected cells should not only realize the transgene's functionality but also maintain their original functionality in vivo (*18*, *26*). To verify that the cells after acoustothermal transfection can realize both the transgene and their original functions, in vivo experiments were performed by injecting MSCs transfected with CXCR4 into mice and then examining the distribution of transfected MSCs and their functions.

It is critical that the MSCs treated by acoustothermal transfection can exert their original therapeutic function. To test this original functionality, a MCAO mouse model was established, then MSCs (~3×10^6) transfected with CXCR4 were injected into the MCAO mice via a tail vein, and after injection, in vivo imaging system (IVIS) and magnetic resonance imaging (MRI) were conducted (as shown in Fig. 5, A and B). The MSCs transfected with CXCR4 showed highly efficient homing effects to cerebral ischemic injury, as indicated by the strong fluorescence in IVIS images acquired on day 1 after injection (Fig. 5C). The maximum fluorescence intensity was achieved on day 5 after injection (Fig. 5D). The good homing effects of the transfected MSCs improved the therapeutic effect of MCAO. Moreover, MRI was used to evaluate the infarct volume change after the injection of transfected MSCs. The MRI results

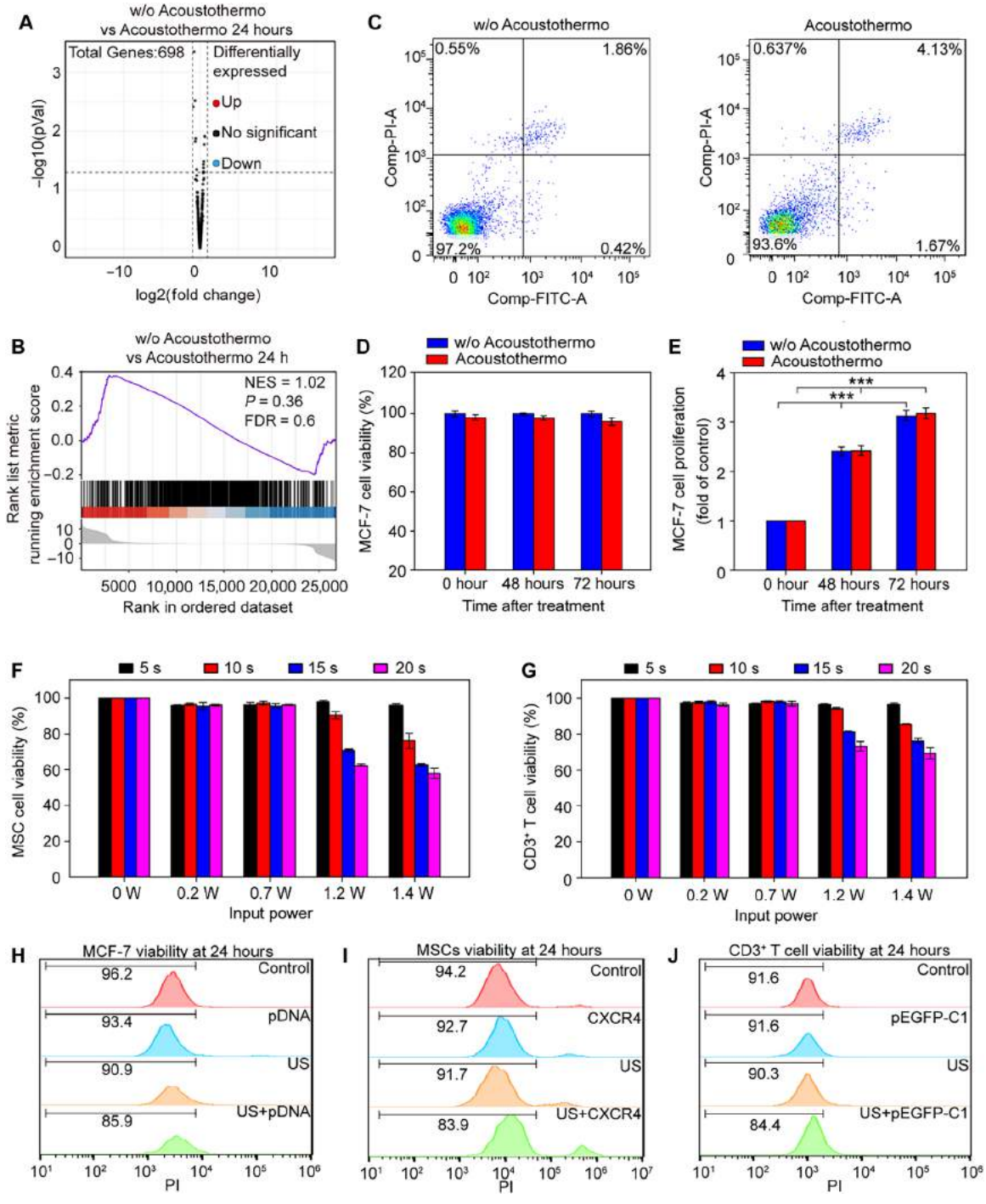

Fig. 4. Biocompatibility evaluation on the transcriptome and cell viability level. Characterization results for (**A**) differential expression analysis of RNA damage genes, (**B**) GSEA analysis of differential expression genes, and (**C**) cell viability characterized by flow cytometry at 48 hours. Cells from three repeated experiments were assigned for the flow cytometry. (**D**) Viability of MCF-7 cells characterized by CCK-8 assays. (**E**) Cell proliferative activity is characterized by CCK-8 assays. In all the figures, results for cases without and with acoustothermal treatment are provided. Five repeated experiments were included in the statistical analysis. (**F**) Viability of MSCs characterized by CCK-8 assays 24 hours after acoustothermal treatment. (**G**) Viability of $CD3^+$ T cells characterized by CCK-8 assays 24 hours after acoustothermal treatment. (**H** to **J**) Viability of MCF-7 cells, MSC cells, and $CD3^+$ T cells in the presence of plasmids characterized by flow cytometry 24 hours after acoustothermal treatment.

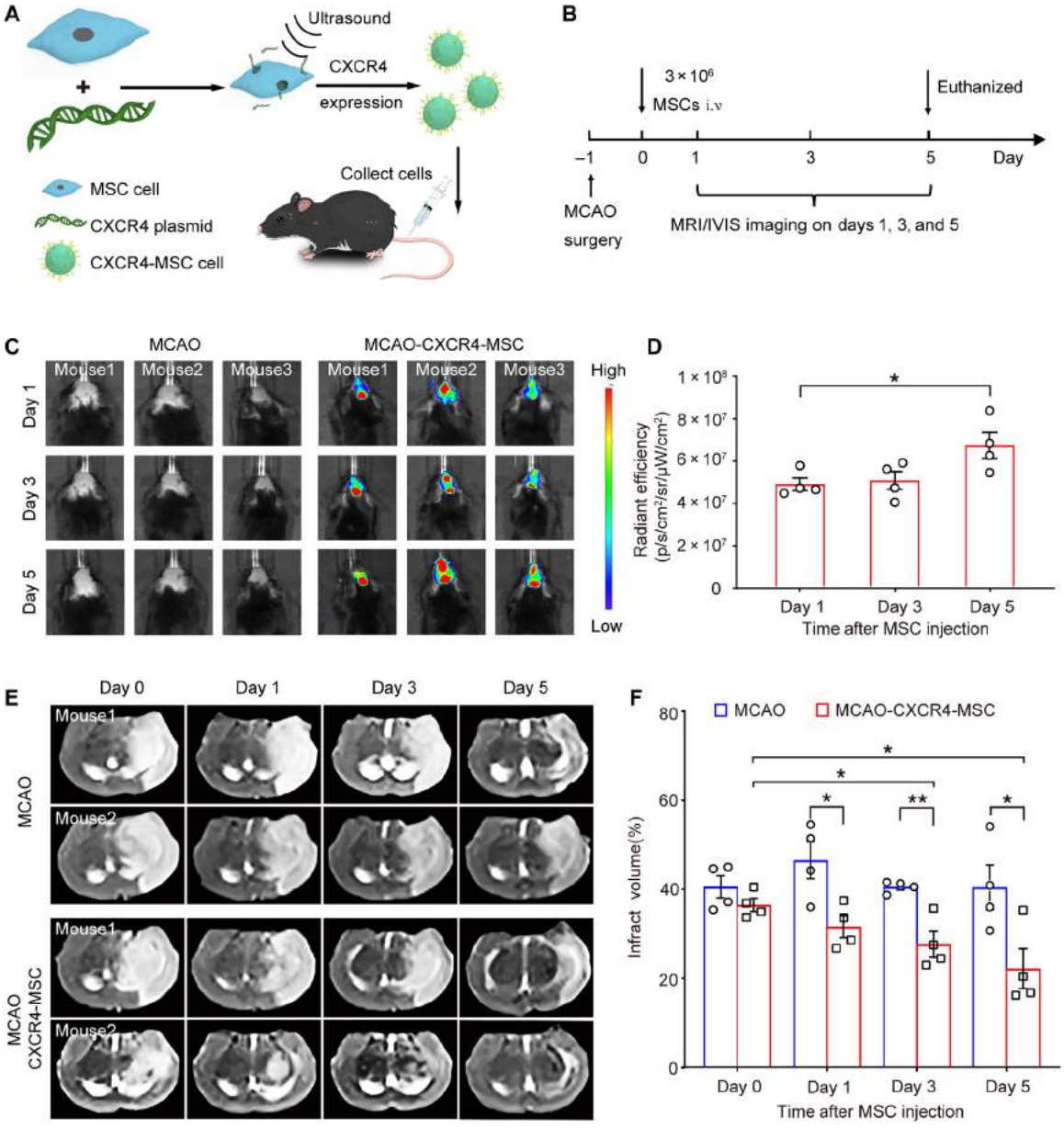

Fig. 5. In vivo studies of MSCs transfected with CXCR4 via the acoustothermal method. (**A**) Schematics showing the process of delivering CXCR4 into MSCs using the acoustothermal transfection method and further injecting the CXCR4-MSCs into MCAO mice for cerebral ischemia treatment. (**B**) A schedule of using MSCs transfected with CXCR4 for the cell therapy of MCAO mice. (**C**) IVIS imaging for characterizing the distributions of CXCR4-MSCs with 1,1′-dioctadecyl-3,3,3′,3′-tetramethylindotricarbocyanine (DiR)–labeled in the cerebral ischemic area over time. The acquired images show that the transfected MSCs gradually aggregate at the infarct site over time. (**D**) Quantitative characterization results showing the accumulation of MSCs over time. (**E**) MRI images captured on different days for characterizing the infarct area size (white area) after CXCR4-MSC treatment. (**F**) Quantitative characterization results of infarct volume ratios over time. The days 3 and 5 results for groups injected with transfected MSCs show significant reductions in infarct volumes, compared to the results of the MCAO group.

(Fig. 5, E and F) show that the infarct volume ratio gradually decreased from 36.5 ± 1.5% to 22.2 ± 4.5% in 5 days after injecting with transfected MSCs, whereas the infarct volume ratio in the control group without injecting transfected MSCs remained almost the same (from 40.6 ± 2.5% to 40.5 ± 5.0%). The significant reduction of the infarct volume was confirmed by both the 2,3,5-triphenyltetrazolium hydrochloride (Sigma-Aldrich) and hematoxylin and eosin (section S1) staining results (figs. S21 and S22).

As other studies (*6*) reported, MSCs can increase the level of BDNF protein in the lesion area and further reduce neuronal apoptosis, which is the candidate mechanism to treat ischemic stroke using MSCs. The immunofluorescence staining results of NeuN and BDNF proteins demonstrated that CXCR4-MSC can increase the related protein expression (fig. S23). These results verify that the MSCs transfected with CXCR4 by our acoustothermal transfection method can efficiently aggregate in the ischemic region of the brain

cortex, further reducing the infarct volumes via increasing the expression of BDNF and NeuN. These results also confirm that MSCs treated with acoustothermal transfection can maintain their therapeutic functionality in vivo and can be used for cell therapy in vivo.

DISCUSSION

In this study, we developed and validated an acoustothermal transfection technique for enabling efficient and high-throughput transfection of hard-to-transfect cells, including stem and primary T cells, by enhancing both the cell membrane and nuclear envelope transient permeabilities. In particular, the acoustothermal transfection technique distinguishes itself from previous ultrasonic transfection methods by leveraging high-frequency SAW-induced acoustic and thermal effects on cells, i.e., using acoustic forces to perforate cells and, meanwhile, leveraging thermal effects induced by the viscous damping of acoustic waves to allow the lipid membrane to more easily be permeabilized. On the basis of both the acoustic and thermal effects, our acoustothermal transfection method allows for fast, efficient, and simultaneous delivery of multiple types of large functional cargos into the cytoplasm and nucleus.

To understand the biophysical mechanisms of acoustothermal transfection, we performed a series of simulations and experiments. The results show that our acoustothermal transfection device can generate standing acoustic waves with displacements near 4 nm on the top surface of a PDMS layer and apply both acoustic radiation forces and acoustic streaming shear forces on cells. The application of SAWs increases the time-average temperature to 42°C in 10 s through the viscous damping of acoustic waves, and it is free of cavitation because neither higher harmonic frequencies generated by stable cavitation nor broadband noise resulting from microbubble collapse during the inertial cavitation were detected. These results indicate that our acoustothermal transfection method leverages the combined acoustic and thermal effects on cells. Through comparison experiments, we confirmed that the combined acoustic and thermal effects could significantly enhance the cell membrane permeability for efficient cargo delivery; however, the sole acoustic or thermal effect led to much lower delivery efficiencies. In Fig. 2G and fig. S7, we found that solely the acoustic effect was capable of inducing cell perforation, albeit with a relatively low efficiency of 20.5 ± 0.7% when prolonging the stimulation time to 30 s. Previous studies also have demonstrated that the sole mechanical effect of ultrasound enables generation of transient gaps between the lipid molecules of the membrane to enhance the membrane permeability (*60*, *61*).

Our device used a PDMS layer to partially absorb the acoustic energy and facilitate its conversion into thermal energy, resulting in the temperature elevation. The thermal effect may play a crucial role in transforming the cell membrane to a colloidal state and thus enhances the fluidity of membrane lipids (*62*). To verify this hypothesis, dipalmitoylphosphatidylcholine (DPPC) vesicles, with a phase-transition temperature of 41°C, were fabricated to mimic the cell membrane's reaction to acoustothermal treatment. The preparation of DPPC vesicles is in the section S2. The results verified that the acoustic thermal effect enabled enhancement of membrane permeability by transforming the lipid bilayers into a colloidal state (fig. S24). The colloid state reduces the force threshold to generate transient pores, thus facilitating the delivery of large cargos into cells (fig. S25). Moreover, the gradient of the temperature distribution in the fluid medium (fig. S6) was capable of generating the thermophoretic force (*63*–*65*) that may contribute to improving membrane permeability.

In addition, the establishment of the standing waves enables improvement of the mechanical effects of the ultrasound due to a significantly larger pressure gradient compared to the traveling waves. In the Rayleigh domain ($kR << 1$), where k is the wave number and R is the characteristic size of the cell, the acoustic radiation force on a cell is proportional to the gradient of the acoustic potential (section S3). For a cell with a diameter of 20 μm, the maximum acoustic radiation force on the cell was 78 nN in standing waves and 9 pN in traveling waves. This indicates that the cell experiences an acoustic force in standing waves that is almost four orders of magnitude larger than that in traveling waves. In addition, the shear force on the cells is also proportional to the gradient of the acoustic pressure. The shear stress is approximately two orders larger than that of traveling waves. The larger acoustic radiation force and shear force in standing waves assist in enhancing the membrane permeability (fig. S26).

On the basis of further experiments, we found the that perforation efficiency is highly related to the heating rate ($\Delta T/\Delta t$) and the heating rate may be regarded as an important indicator for acoustothermal sonoporation. The relationship between the perforation efficiency and viability and heating rate for MCF-7 and MSC cells is depicted in fig. S27. The measured temperature was on the top surface of the PDMS layer using an infrared thermal imager. As the heating rate increased, the sonoporation efficiency was improved significantly, while decreased viability of cells was observed. The fitting curve of perforation efficiency, represented by the red line in fig. S27 (A and C), exhibited a relatively wide full width at half maximum (FWHM) for MCF-7 cells compared to MSC cells. For MCF-7 cells, a high perforation efficiency could be achieved when the heating rate ranged from 0.64° to 2.98°C/s. These results indicated that, when the treatment time was 10 s, the temperature elevation between 6.4° and 29.8°C was capable of realizing the uniform perforation (fig. S8). However, when the heating rate exceeded 2.98°C/s, a considerable number of cells were dead after acoustothermal treatment (fig. S27B). Figure S27 (C and D) demonstrates that MSC cells exhibited a narrow FWHM in perforation, with an effective region ranging from 0.87° to 2.04°C/s.

Our study validates that acoustothermal transfection holds multiple desired features for gene and cell therapies. (i) It allows for delivering multiple types of large cargos into nuclei within a short amount of time (~5 min) and achieves efficient gene expression within 14 hours. (ii) It can be easily scaled up for achieving high throughputs, by integrating multiple independent acoustothermal transfection units. For example, our fabricated device with 6 × 8 units (Fig. 1A) enabled the transfection of ~1.7 million cells within 1 min with a high gene expression efficiency of 93.9 ± 3.6% and 85.0 ± 0.6% for delivering a single type of plasmids into MSCs and T cells, respectively. (iii) It can simultaneously deliver multiple types of plasmids into hard-to-transfect cells with high efficiency. As validated by our experiments, dual types of plasmids could be delivered into MSCs with dual gene expression efficiencies of 89.6 ± 1.2% (89.4% with flow cytometry). We expect that this feature can benefit the delivery of CRISPR-Cas9 systems into CAR-T cells for cell therapy. (iv) It has high biocompatibility for the long-term growth of treated cells, as proven by our characterization results with no obvious gene mutation (Fig. 4, A and B) and high cell viability (85.9% in Fig. 4H). (v) Cells treated by acoustothermal transfection can realize the transgene's functionality and maintain their original functionality

in vivo. As demonstrated by cerebral ischemia therapy experiments, after transfecting MSCs with CXCR4 gene using acoustothermal transfection and injecting transfected MSCs into MCAO mice, the overexpression of CXCR4 gene enabled substantial accumulation of transfected MSCs in the ischemic area. Moreover, the ischemic volume was greatly reduced in 5 days after injection with the aforementioned critical features. In the long run, we expect that our developed acoustothermal transfection device can serve as a robust, portable, and easy-to-use tool for biomedical research and clinical applications.

MATERIALS AND METHODS

Fabrication of acoustothermal transfection arrays

Figure 1A and fig. S1 show a schematic and an image of our developed acoustothermal transfection array with 6 × 8 units. Each unit is composed of IDTs for generating SAWs, a PDMS (Sylgard184, Dow Corning, USA) well for hosting cells, and a 1-mm-thick PDMS layer covering the IDTs. This PDMS layer is for delivering acoustic energy to cells in the PDMS well and converting a portion of acoustic energy to thermal energy through viscous damping. Each IDTs, with an electrode thickness of 500 nm, was sputtered on a 128° Y-cut lithium niobate ($LiNbO_3$) substrate. Each IDT's finger electrodes have a width and a spacing of 40 μm, for achieving a resonant frequency of 24 MHz. The acoustic aperture of each IDT is 4.8 mm to cover the sonoporation well. During the fabrication process, multiple IDTs in an array were fabricated on a $LiNbO_3$ wafer and divided into individual elements using a scribing machine. Then, a single element was adhered to a customized polychlorinated biphenyl that can mitigate the acoustic and electrical cross-talk. The PDMS well was fabricated by pouring a viscous mixture (10:1 base-to-curing agent ratio) into an acrylic mold. After baking them at 80°C for 40 min, the PDMS was peeled from the mold and bonded on the $LiNbO_3$ substrate. The radius, height, and bottom thickness of the fabricated PDMS well were 4, 5, and 1 mm, respectively. After device fabrication, a network analyzer (E5061B, KEYSIGHT, USA) was adopted to characterize the resonant frequency of each IDTs. To use the fabricated device for gene delivery, a signal containing continuous sine waves at the resonant frequency was generated by a function generator (AFG 3102, Tektronix, USA), further amplified by a power amplifier (100A400A, Amplifier Research, USA), and then sent to the IDTs for generating SAWs.

Characterization of displacements, temperature changes, and cavitation induced by SAWs

In each unit of our array, the energy of standing SAWs generated by IDTs can transmit to a thin PDMS layer (i.e., a PDMS well's bottom) covering the IDTs. Moreover, a portion of acoustic energy can convert to thermal energy because of the PDMS's viscous damping. To better understand the mechanisms of our acoustothermal transfection device, we performed a series of experiments to characterize the displacement fields, temperature changes, and cavitation induced by our acoustothermal transfection device.

To characterize the out-of-plane displacement field on the top surface of a PDMS layer covering IDTs, a laser Doppler vibrometer (UHF-120, Polytec GmbH, Germany) was used. The laser beam was focused on the top surface of the PDMS layer and set to a direction that is perpendicular to the top surface, to measure the SAW-induced out-of-plane displacement based on the Doppler effect. By scanning the area of interest through a point-by-point manner, a two-dimensional (2D) displacement field was acquired as shown in Fig. 2A. In addition to using the laser Doppler vibrometer, we used acoustic wave–induced particle distributions for device characterization. A 10-μl solution containing polystyrene particles with a diameter of 5 μm (or 2 μm) was added to a PDMS well for characterizing the acoustic radiation force (or acoustic streaming) induced by SAWs. The acquired distributions of 5- and 2-μm polystyrene particles are given in Fig. 2 (B and C, respectively).

To investigate whether acoustic cavitation is induced by our device, the frequency spectrum in the PDMS well was measured during SAW generation. Since acoustic cavitation can induce harmonic frequency components or wide band noises, the acquired frequency spectrum can indicate whether acoustic cavitation is introduced. Our measured spectrum in Fig. 2D only has one strong peak at the SAW excitation frequency without high harmonic components or wide band noises. This observation indicates our acoustothermal transfection device is free of acoustic cavitation.

To characterize temperature increases induced by our acoustothermal transfection device through the viscous damping of acoustic waves, 2D temperature fields on the PDMS surface were monitored by an infrared thermal imager (R300, NEC Avio, Tokyo, Japan) with a resolution of 0.1°C. Time-average temperature in the cell culture space that was quantified from fig. S6 shows the acquired spatial temperature fields at different times during SAW generation.

Numerical simulations

Numerical simulations were performed using finite element software COMSOL Multiphysics 5.4 (COMSOL Co. Ltd.). The piezoelectric device module that couples the solid mechanics and electrostatics governing equations was adopted to simulate the generation of SAWs (*66*). The thermoviscous acoustics module was used for simulating pressure acoustic waves in the PDMS layer and the viscous damping–induced temperature changes.

Cell culture

MCF-7 human breast cells were obtained from the Cell Resource Center of the Chinese Academy of Science, China. Bone marrow MSCs of C57BL/6J mice were obtained from Cyagen Biosciences (Cyagen Biosciences Inc., China). These cells were cultured in an incubator with a humidified atmosphere containing 5% CO_2 at 37°C. Primary human $CD3^+$ T cells were purchased from Milestone (Shanghai) Biological Science & Technology Co. Ltd. Before transfection, the isolated $CD3^+$ T cells were stimulated for 2 days in RPMI 1640 medium (11875093, Thermo Fisher Scientific, USA) and anti-human CD3/CD28 magnetic dynabeads (11132D, Gibco, USA) at a bead-to-cell concentration of 1:1, along with a cytokine cocktail of interleukin-2 (IL-2) at (50 U/ml; 200-02, PeproTech, USA). Then, the magnetic dynabeads were removed by Easysp Magent (18000, Stemcell Technologies, Canada). Following transfection, the peripheral blood mononuclear cells were incubated in an RPMI 1640 medium with IL-2 (50 U/ml).

To obtain stably growing cells on the PDMS surface for a consistent transfection effect, poly-L-lysine (P4017, Sigma-Aldrich, USA) was injected into the PDMS wells to incubate for 30 min at 37°C, which facilitated cell adhesion. Before acoustothermal transfection treatment, MCF-7 cells or MSCs at a density of 3×10^5 cells/ml were cultured in the self-manufactured PDMS well for 24 hours. The $CD3^+$ T cells at a density of 3×10^5 cells/ml sank to the PDMS bottom surface and adhered after cultured for 4 hours.

Characterization of cell perforation/transfection efficiency and viability

To characterize cell membrane permeability changes, PI (P4170, Sigma-Aldrich, USA), and calcein-AM (56496, Sigma-Aldrich, USA) were added to a phosphate-buffered saline (PBS; 14040133, Gibco, USA) containing cells. After SAW treatment, the perforated live cells (counted for N1) had both the PI and calcein-AM fluorescence. The live cells (counted for N2) were brightened in the calcein-AM fluorescence. The perforation efficiency was calculated by N1/N2 (%). In addition, flow cytometry was performed to statistically characterize the perforation efficiency.

To assess the biocompatibility of our acoustothermal transfection method, flow cytometry was performed to characterize cell apoptosis, with the assistance of an annexin V–fluorescein isothiocyanate/PI apoptosis kit (KGA107, Keygen, China). Cell viability was characterized by using a cell counting kit-8 (CCK-8, C0041, Beyotime, China) after acoustothermal transfection treatment according to the manufacturer instruction. Cell viability was calculated by using absorbance of the experimental well dividing control absorbance. The calcein-AM/PI (40747ES76, Yesen, China) staining was performed to observe live (indicated by calcein-AM) and dead (indicated by PI) cells.

Flow cytometry was applied to further estimate the long-term viability after pDNA transfection. For MCF-7, MSC, and $CD3^+$ T cells transfected with CXCR4, EGFP excited by 488 nm was applied to indicate the target gene expression; thus, PI excited by 561 nm was used as the effective marker to estimate the dead cells. In the viability test, the DNA plasmids were incubated together with the transfected cells. Before acoustothermal transfection treatment, MCF-7 cells or MSCs at a density of 3×10^5 cells/ml were cultured in the self-manufactured PDMS well for 24 hours. The $CD3^+$ T cells at a density of 3×10^5 cells/ml sank to the PDMS bottom surface and adhered after cultured for 4 hours. Acoustothermal treatment (input power = 1.2 W and treatment time = 10 s) was applied to conduct gene transfection immediately after 100 ng of pDNA was mixed with the adhered cells in the PDMS chamber. After cultured for 24 hours, cells were digested with 0.25% trypsin and centrifugated. Then after incubation with PI in a dark environment, cells were characterized by flow cytometry (CytoFLEX S, Beckman, USA).

Delivery of CdTe quantum dots and carbon nanoparticles to MCF-7 cells

The CdTe quantum dots (average diameter, 6.74 nm) were synthesized following a typical protocol reported in previous studies (*67*). To obtain an effective cell adhesion, 10 μl of polylysine was incubated for 30 min and washed twice with PBS before MCF-7 cells were harvested and plated into the PDMS well. To deliver CdTe quantum dots to MCF-7 cells, a solution containing CdTe quantum dots (0.1 mg/ml) was added into MCF-7 cells (10 μl per well with a concentration of 3×10^2 cells/μl) adhered to a PDMS well of our device and then the SAWs were turned on for 10 s. In addition, we used our method to deliver carbon nanoparticles (900414, Sigma-Aldrich, USA) with a diameter of 43.5 nm to MFC-7 cells, to investigate the capability of directly and quickly transporting functional large cargos to cell nuclei by enhancing the nuclear envelope permeability. To characterize the post treatment results, the cells were washed with a PBS buffer twice and then imaged under an inverted microscope (Axio Observer Z1, Zeiss, Germany).

Delivery of plasmids into MCF-7 cells, MSCs, and $CD3^+$ T cells

To investigate the capability of our acoustothermal transfection device for delivering plasmids to different types of cells, we performed multiple transfection experiments using our method. First, the plasmids encoding FUGW-pCMV-RRE-EGFP (9951 bp, 6.5 MDa, denoted as PUGW-EGFP) were chosen for the transfection of MCF-7 cells. Second, the plasmid encoding EF1α-BDNF-mCherry (6859 bp, 4.5 MDa, denoted as BDNF) and the plasmid encoding CXCR4-pEF1α-IRES-AcGFP (7107 bp, 4.6 MDa, denoted as CXCR4) were used, to investigate the capability of our acoustothermal transfection device for delivering two different types of plasmids into MSCs individually and simultaneously. Third, the pEGFP-C1 plasmid (4731 bp, 3 MDa, denoted as EGFP) was used for the transfection of $CD3^+$ T cells. Before each acoustothermal transfection experiment, a 10-μl fresh basic minimum essential medium (MEM) containing 0.5 μg of pDNA was added to a PDMS well of our device. All three pDNAs (CXCR4, BDNF, and EGFP) concentrations are 10 ng/μl. After acoustothermal transfection treatment, the cells were added to their corresponding culture media and cultured in an incubator. At 14 and 24 hours after acoustothermal transfection treatment, cells were fixed and stained for characterizing the gene expression using confocal microscopy imaging.

For comparison, MSCs and $CD3^+$ T cells were also transfected by electroporation (4D-Nucleofector Core Unit, Lonza, USA). A P1 primary 4D-Nucleofector X kit (PBP1-00675, 20 μl) was used for the transfection of MSCs and a P1 primary 4D-Nucleofector X kit (PBP3-00675, 20 μl) was adopted for the transfection of $CD3^+$ T cells. These transfection experiments were conducted under the guidance of a Lonza technician following a protocol provided by Lonza.

RNA sequencing

The MCF-7 cells were collected for RNA sequencing at 24 hours after acoustothermal transfection treatment. The total RNA was extracted using a TRIzol reagent (Invitrogen, CA, USA). The total RNA quantity and purity were analyzed using the Bioanalyzer 2100 system and the RNA 6000 Nano Lab Chip Kit (Agilent, CA, USA) with an RNA integrity number > 7.0. Approximately 10 μg of total RNA, which represented a specific adipose type, was exposed to isolate poly(A) mRNA with poly-T oligo attached magnetic beads (Invitrogen, CA, USA). After purification, divalent cations at an increased temperature were used to fragment the mRNA. Subsequently, the cleaved RNA fragments underwent reverse transcription to generate the cDNA library according to the mRNA-Seq sample preparation kit (Illumina, San Diego, USA) protocol. Three hundred base pairs (±50 bp) were the average insert size for the paired-end libraries. After sample preparation, paired-end sequencing was performed on an Illumina sequence platform.

Animal experiments

All animal experiments were carried out strictly according to the procedures required by the Chinese Academy of Sciences Animal Care and Use Committee. C57BL/6J mice (male, 7 weeks old, weighing 18 to 22 g) were obtained from Beijing Vital River Laboratory Animal Technology Co. Ltd. The MCAO model establishment details are in the section S4.

MRI imaging

A clinical MRI system (Magneton TIM Trio, Siemens) was used for the MRI imaging of the mouse cerebral infarction area and confirming the success of constructing the MCAO model mice at 12 hours

after MCAO surgery. The MCAO mice were randomly divided into two groups: a CXCR4-MSC group (MCAO mice treated with CXCR4-MSCs, $n = 4$) and a control group (MCAO mice without any treatment, $n = 4$). On day 1 after the MCAO surgery, MSCs (3×10^6 cells) were injected into each mouse via the tail intravenous injection.

Infarct volume development was assessed on days 1, 3, and 5 after the CXCR4-MSC injection using MRI. A contiguous set of axial imaging slices (17 slices, 1 mm thick, T2 weighted) containing the ischemic region was acquired using a fast spin-echo sequence to delineate the anatomical details (field of view = 60 mm, in-plane resolution of 250 μm, echo time = 94 ms, repetition time = 4935 ms, echo train length = 16, and number of averages = 6). These images were further analyzed for determining the infarct volume ratio ($V_{\text{ischemic}}/V_{\text{whole brain}} \times 100\%$).

IVIS for characterizing the CXCR4-MSC accumulation

For in vivo characterization of the CXCR4-MSC accumulation, a near-infrared dye 1,1′-dioctadecyl-3,3,3′,3′-tetramethylindotricarbocyanine [DiR, DiIC18(7), MKBio, China] was used as a marker. The collected MSCs or CXCR4-MSCs were added with a basal Dulbecco's MEM containing 20 μg of DiR near-infrared dye and stained for 15 min. After washing the stained cells three times using PBS, the cells were suspended in a 0.85% NaCl solution to a density of 3×10^8 cells/ml. After the MSC injection, fluorescence imaging of the mice was performed on days 0, 1, 3, and 5 using an IVIS (Caliper IVIS Spectrum, PerkinElmer, USA; excitation, 745 nm; emission, 800 nm).

Data analysis

All the data were obtained from at least three independent experiments. Statistical analysis was carried out with OriginPro2018 version SR1 (Origin OriginLab, Northampton, MA). After a Shapiro-Wilk test for estimating if the data obey a normal distribution, an unpaired Student's t test was applied to compare two groups of data that obey normal distribution. One-way analysis of variance was applied followed by Tukey's multiple comparisons test. Mean ± SEM is presented in all data. $^*P < 0.05$, $^{**}P < 0.01$, and $^{***}P < 0.001$.

Supplementary Materials

This PDF file includes:
Sections S1 to S4
Figs. S1 to 27
Legends for movies S1 to S3

Other Supplementary Material for this manuscript includes the following:
Movies S1 to S3

REFERENCES AND NOTES

1. K. Adachi, Y. Kano, T. Nagai, N. Okuyama, Y. Sakoda, K. Tamada, IL-7 and CCL19 expression in CAR-T cells improves immune cell infiltration and CAR-T cell survival in the tumor. *Nat. Biotechnol.* **36**, 346–351 (2018).
2. K. A. High, M. G. Roncarolo, Gene Therapy. *N. Engl. J. Med.* **381**, 455–464 (2019).
3. M. Cavazzana, F. D. Bushman, A. Miccio, I. Andre-Schmutz, E. Six, Gene therapy targeting haematopoietic stem cells for inherited diseases: Progress and challenges. *Nat. Rev. Drug Discov.* **18**, 447–462 (2019).
4. J. Lee, K. Henderson, M. W. Massidda, M. Armenta-Ochoa, B. G. Im, A. Veith, B.-K. Lee, M. Kim, P. Maceda, E. Yoon, L. Samarneh, M. Wong, A. K. Dunn, J. Kim, A. B. Baker, Mechanobiological conditioning of mesenchymal stem cells for enhanced vascular regeneration. *Nat. Biomed. Eng.* **5**, 89–102 (2021).
5. H. Li, Y. Yang, W. Hong, M. Huang, M. Wu, X. Zhao, Applications of genome editing technology in the targeted therapy of human diseases: Mechanisms, advances and prospects. *Signal Transduct. Target. Ther.* **5**, 1 (2020).
6. G. L. Zhang, Z. H. Zhu, Y. Z. Wang, Neural stem cell transplantation therapy for brain ischemic stroke: Review and perspectives. *World J. Stem Cells* **11**, 817–830 (2019).
7. X.-C. Jiang, J.-J. Xiang, H.-H. Wu, T.-Y. Zhang, D.-P. Zhang, Q.-H. Xu, X.-L. Huang, X.-L. Kong, J.-H. Sun, Y.-L. Hu, K. Li, Y. Tabata, Y.-Q. Shen, J.-Q. Gao, Neural stem cells transfected with reactive oxygen species-responsive polyplexes for effective treatment of ischemic stroke. *Adv. Mater.* **31**, e1807591 (2019).
8. L. Cong, F. A. Ran, D. Cox, S. Lin, R. Barretto, N. Habib, P. D. Hsu, X. Wu, W. Jiang, L. A. Marraffini, F. Zhang, Multiplex genome engineering using CRISPR/Cas systems. *Science* **339**, 819–823 (2013).
9. N. S. McCarty, A. E. Graham, L. Studena, R. Ledesma-Amaro, Multiplexed CRISPR technologies for gene editing and transcriptional regulation. *Nat. Commun.* **11**, 1281 (2020).
10. L. Y. Guo, J. Bian, A. E. Davis, P. Liu, H. R. Kempton, X. Zhang, A. Chemparathy, B. Gu, X. Lin, D. A. Rane, X. Xu, R. M. Jamiolkowski, Y. Hu, S. Wang, L. S. Qi, Multiplexed genome regulation in vivo with hyper-efficient Cas12a. *Nat. Cell Biol.* **24**, 590–600 (2022).
11. Z. X. Chong, S. K. Yeap, W. Y. Ho, Transfection types, methods and strategies: A technical review. *PeerJ* **9**, e11165 (2021).
12. H. Bai, G. M. S. Lester, L. C. Petishnok, D. A. Dean, Cytoplasmic transport and nuclear import of plasmid DNA. *Biosci. Rep.* **37**, (2017).
13. C. M. Roberts, E. S. Ratner, "Two Plasmid-Based Systems for CRISPR/Cas9 Mediated Knockout of Target Genes" in *Detection of Cell Death Mechanisms: Methods and Protocols*, A. B. Alvero, G. G. Mor, Eds. (Springer US, New York, NY, 2021), pp. 213–232.
14. L. Labanieh, R. G. Majzner, D. Klysz, E. Sotillo, C. J. Fisher, J. G. Vilches-Moure, K. Z. B. Pacheco, M. Malipatlolla, P. Xu, J. H. Hui, T. Murty, J. Theruvath, N. Mehta, S. A. Yamada-Hunter, E. W. Weber, S. Heitzeneder, K. R. Parker, A. T. Satpathy, H. Y. Chang, M. Z. Lin, J. R. Cochran, C. L. Mackall, Enhanced safety and efficacy of protease-regulated CAR-T cell receptors. *Cell* **185**, 1745–1763.e22 (2022).
15. M. Hong, J. D. Clubb, Y. Y. Chen, Engineering CAR-T cells for next-generation cancer therapy. *Cancer Cell* **38**, 473–488 (2020).
16. M. P. Stewart, A. Sharei, X. Ding, G. Sahay, R. Langer, K. F. Jensen, In vitro and ex vivo strategies for intracellular delivery. *Nature* **538**, 183–192 (2016).
17. L. Raes, S. C. D. Smedt, K. Raemdonck, K. Braeckmans, Non-viral transfection technologies for next-generation therapeutic T cell engineering. *Biotechnol. Adv.* **49**, 107760 (2021).
18. A. M. Vargason, A. C. Anselmo, S. Mitragotri, The evolution of commercial drug delivery technologies. *Nat. Biomed. Eng.* **5**, 951–967 (2021).
19. J. L. Young, D. A. Dean, Electroporation-mediated gene delivery. *Adv. Genet.* **89**, 49–88 (2015).
20. T. DiTommaso, J. M. Cole, L. Cassereau, J. A. Bugge, J. L. S. Hanson, D. T. Bridgen, B. D. Stokes, S. M. Loughhead, B. A. Beutel, J. B. Gilbert, K. Nussbaum, A. Sorrentino, J. Toggweiler, T. Schmidt, G. Gyuelveszi, H. Bernstein, A. Sharei, Cell engineering with microfluidic squeezing preserves functionality of primary immune cells in vivo. *Proc. Natl. Acad. Sci. U.S.A.* **115**, E10907–E10914 (2018).
21. A. Tay, The benefits of going small: Nanostructures for mammalian cell transfection. *ACS Nano* **14**, 7714–7721 (2020).
22. C. J. Bishop, S. Y. Tzeng, J. J. Green, Degradable polymer-coated gold nanoparticles for co-delivery of DNA and siRNA. *Acta Biomater.* **11**, 393–403 (2015).
23. M. S. Shim, Y. J. Kwon, Dual mode polyspermine with tunable degradability for plasmid DNA and siRNA delivery. *Biomaterials* **32**, 4009–4020 (2011).
24. M. P. Stewart, R. Langer, K. F. Jensen, Intracellular delivery by membrane disruption: Mechanisms, strategies, and concepts. *Chem. Rev.* **118**, 7409–7531 (2018).
25. A. Tay, N. Melosh, Nanostructured materials for intracellular cargo delivery. *Acc. Chem. Res.* **52**, 2462–2471 (2019).
26. J. Hur, A. J. Chung, Microfluidic and nanofluidic intracellular delivery. *Adv. Sci.* **8**, e2004595 (2021).
27. J. J. VanDersarl, A. M. Xu, N. A. Melosh, Nanostraws for direct fluidic intracellular access. *Nano Lett.* **12**, 3881–3886 (2012).
28. V. M. Kadiri, C. Bussi, A. W. Holle, K. Son, H. Kwon, G. Schütz, M. G. Gutierrez, P. Fischer, Biocompatible magnetic micro- and nanodevices: Fabrication of FePt nanopropellers and cell transfection. *Adv. Mater.* **32**, e2001114 (2020).
29. A. Sharei, J. Zoldan, A. Adamo, W. Y. Sim, N. Cho, E. Jackson, S. Mao, S. Schneider, M.-J. Han, A. Lytton-Jean, P. A. Basto, S. Jhunjhunwala, J. Lee, D. A. Heller, J. W. Kang, G. C. Hartoularos, K.-S. Kim, D. G. Anderson, R. Langer, K. F. Jensen, A vector-free microfluidic platform for intracellular delivery. *Proc. Natl. Acad. Sci. U.S.A.* **110**, 2082–2087 (2013).
30. D. Morshedi Rad, M. Alsadat Rad, S. Razavi Bazaz, N. Kashaninejad, D. Jin, M. Ebrahimi Warkiani, A comprehensive review on intracellular delivery. *Adv. Mater.* **33**, e2005363 (2021).
31. C. Chiappini, E. De Rosa, J. O. Martinez, X. Liu, J. Steele, M. M. Stevens, E. Tasciotti, Biodegradable silicon nanoneedles delivering nucleic acids intracellularly induce localized in vivo neovascularization. *Nat. Mater.* **14**, 532–539 (2015).
32. M. E. Kizer, Y. Deng, G. Kang, P. E. Mikael, X. Wang, A. J. Chung, Hydroporator: A hydrodynamic cell membrane perforator for high-throughput vector-free nanomaterial intracellular delivery and DNA origami biostability evaluation. *Lab Chip* **19**, 1747–1754 (2019).

33. Y. Deng, M. Kizer, M. Rada, J. Sage, X. Wang, D. J. Cheon, A. J. Chung, Intracellular delivery of nanomaterials via an inertial microfluidic cell hydroporator. *Nano Lett.* **18**, 2705–2710 (2018).
34. J. A. Jarrell, A. A. Twite, K. H. W. J. Lau, M. N. Kashani, A. A. Lievano, J. Acevedo, C. Priest, J. Nieva, D. Gottlieb, R. S. Pawell, Intracellular delivery of mRNA to human primary T cells with microfluidic vortex shedding. *Sci. Rep.* **9**, 3214 (2019).
35. X. Xing, Y. Pan, L. Yobas, A low-backpressure single-cell point constriction for cytosolic delivery based on rapid membrane deformations. *Anal. Chem.* **90**, 1836–1844 (2018).
36. R. Kusters, T. van der Heijden, B. Kaoui, J. Harting, C. Storm, Forced transport of deformable containers through narrow constrictions. *Phys. Rev. E Stat. Nonlin. Soft Matter Phys.* **90**, 033006 (2014).
37. A. Liu, M. Islam, N. Stone, V. Varadarajan, J. Jeong, S. Bowie, P. Qiu, E. K. Waller, A. Alexeev, T. Sulchek, Microfluidic generation of transient cell volume exchange for convectively driven intracellular delivery of large macromolecules. *Mater. Today* **21**, 703–712 (2018).
38. J. Hur, I. Park, K. M. Lim, J. Doh, S. G. Cho, A. J. Chung, Microfluidic cell stretching for highly effective gene delivery into hard-to-transfect primary cells. *ACS Nano* **14**, 15094–15106 (2020).
39. J. Rufo, F. Cai, J. Friend, M. Wiklund, T. J. Huang, Acoustofluidics for biomedical applications. *Nat. Rev. Methods Primers* **2**, 30 (2022).
40. S. Yang, Z. Tian, Z. Wang, J. Rufo, P. Li, J. Mai, J. Xia, H. Bachman, P.-H. Huang, M. Wu, C. Chen, L. P. Lee, T. J. Huang, Harmonic acoustics for dynamic and selective particle manipulation. *Nat. Mater.* **21**, 540–546 (2022).
41. P. Zhang, H. Bachman, A. Ozcelik, T. J. Huang, Acoustic microfluidics. *Annu. Rev. Anal. Chem.* **13**, 17–43 (2020).
42. J. Rufo, P. Zhang, R. Zhong, L. P. Lee, T. J. Huang, A sound approach to advancing healthcare systems: The future of biomedical acoustics. *Nat. Commun.* **13**, 3459 (2022).
43. P. Fan, Y. Zhang, X. Guo, C. Cai, M. Wang, D. Yang, Y. Li, J. Tu, L. A. Crum, J. Wu, D. Zhang, Cell-cycle-specific cellular responses to sonoporation. *Theranostics* **7**, 4894–4908 (2017).
44. M. T. Burgess, T. M. Porter, Control of acoustic cavitation for efficient sonoporation with phase-shift nanoemulsions. *Ultrasound Med. Biol.* **45**, 846–858 (2019).
45. F. Yang, N. Gu, D. Chen, X. Xi, D. Zhang, Y. Li, J. Wu, Experimental study on cell self-sealing during sonoporation. *J. Control. Release* **131**, 205–210 (2008).
46. L. Meng, X. Liu, Y. Wang, W. Zhang, W. Zhou, F. Cai, F. Li, J. Wu, L. Xu, L. Niu, H. Zheng, Sonoporation of cells by a parallel stable cavitation microbubble array. *Adv. Sci.* **6**, 1900557 (2019).
47. D. Carugo, D. N. Ankrett, P. Glynne-Jones, L. Capretto, R. J. Boltryk, X. Zhang, P. A. Townsend, M. Hill, Contrast agent-free sonoporation: The use of an ultrasonic standing wave microfluidic system for the delivery of pharmaceutical agents. *Biomicrofluidics* **5**, 44108–4410815 (2011).
48. J. Rich, Z. Tian, T. J. Huang, Sonoporation: Past, present, and future. *Adv. Mater. Technol.* **7**, 2100885 (2021).
49. M. S. Gerlt, D. Haidas, A. Ratschat, P. Suter, P. S. Dittrich, J. Dual, Manipulation of single cells inside nanoliter water droplets using acoustic forces. *Biomicrofluidics* **14**, 064112 (2020).
50. J. N. Belling, L. K. Heidenreich, Z. Tian, A. M. Mendoza, T.-T. Chiou, Y. Gong, N. Y. Chen, T. D. Young, N. Wattanatorn, J. H. Park, L. Scarabelli, N. Chiang, J. Takahashi, S. G. Young, A. Z. Stieg, S. De Oliveira, T. J. Huang, P. S. Weiss, S. J. Jonas, Acoustofluidic sonoporation for gene delivery to human hematopoietic stem and progenitor cells. *Proc. Natl. Acad. Sci. U.S.A.* **117**, 10976–10982 (2020).
51. P. Qin, L. Xu, T. Han, L. Du, A. C. H. Yu, Effect of non-acoustic parameters on heterogeneous sonoporation mediated by single-pulse ultrasound and microbubbles. *Ultrason. Sonochem.* **31**, 107–115 (2016).
52. R. Goyal, A. G. Athanassiadis, Z. Ma, P. Fischer, Amplification of acoustic forces using microbubble arrays enables manipulation of centimeter-scale objects. *Phys. Rev. Lett.* **128**, 254502 (2022).
53. M. Maciulevičius, M. Tamošiūnas, D. Navickaitė, S. Šatkauskas, M. S. Venslauskas, Free- and liposomal-doxorubicin delivery via microbubble inertial cavitation. *J. Drug Deliv. Sci. Tech.* **72**, 103386 (2022).
54. U. Farooq, Z. Haider, X. M. Liang, K. Memon, S. M. C. Hossain, Y. Zheng, H. Xu, A. Qadir, F. Panhwar, S. Dong, G. Zhao, J. Luo, Surface-acoustic-wave-based lab-on-chip for rapid transport of cryoprotectants across cell membrane for cryopreservation with significantly improved cell viability. *Small* **15**, e1805361 (2019).
55. C. Cortez-Jugo, S. Masoumi, P. P. Y. Chan, J. Friend, L. Yeo, Nebulization of siRNA for inhalation therapy based on a microfluidic surface acoustic wave platform. *Ultrason. Sonochem.* **88**, 106088 (2022).
56. Y. Q. Fu, J. K. Luo, N. T. Nguyen, A. J. Walton, A. J. Flewitt, X. T. Zu, Y. Li, G. McHale, A. Matthews, E. Iborra, H. Du, W. I. Milne, Advances in piezoelectric thin films for acoustic biosensors, acoustofluidics and lab-on-chip applications. *Prog. Mater. Sci.* **89**, 31–91 (2017).
57. A. Karki, E. Giddings, A. Carreras, D. Champagne, K. Fortner, M. Rincon, J. Wu, Sonoporation as an approach for siRNA delivery into T cells. *Ultrasound Med. Biol.* **45**, 3222–3231 (2019).
58. Z. Fan, H. Liu, M. Mayer, C. X. Deng, Spatiotemporally controlled single cell sonoporation. *Proc. Natl. Acad. Sci. U.S.A.* **109**, 16486–16491 (2012).
59. M. Raab, M. Gentili, H. de Belly, H. R. Thiam, P. Vargas, A. J. Jimenez, F. Lautenschlaeger, R. Voituriez, A. M. Lennon-Dumenil, N. Manel, M. Piel, ESCRT III repairs nuclear envelope ruptures during cell migration to limit DNA damage and cell death. *Science* **352**, 359–362 (2016).
60. S. Ramesan, A. R. Rezk, C. Dekiwadia, C. Cortez-Jugo, L. Y. Yeo, Acoustically-mediated intracellular delivery. *Nanoscale* **10**, 13165–13178 (2018).
61. S. Ramesan, A. R. Rezk, P. M. Cevaal, C. Cortez-Jugo, J. Symons, L. Y. Yeo, Acoustofection: High-frequency vibrational membrane permeabilization for intracellular siRNA delivery into nonadherent cells. *ACS Appl. Bio Mater.* **4**, 2781–2789 (2021).
62. Y. P. Patil, M. D. Kumbhalkar, S. Jadhav, Extrusion of electroformed giant unilamellar vesicles through track-etched membranes. *Chem. Phys. Lipids* **165**, 475–481 (2012).
63. A. Pughazhendi, Z. Chen, Z. Wu, J. Li, Y. Zheng, Opto-thermoelectric tweezers: Principles and applications. *Front. Phys.* **8**, 580014 (2020).
64. Z. Chen, J. Li, Y. Zheng, Heat-mediated optical manipulation. *Chem. Rev.* **122**, 3122–3179 (2022).
65. T. Tsuji, Y. Sasai, S. Kawano, Thermophoretic manipulation of micro- and nanoparticle flow through a sudden contraction in a microchannel with near-infrared laser irradiation. *Phys. Rev. Appl.* **10**, 044005 (2018).
66. Z. Ni, C. Yin, G. Xu, L. Xie, J. Huang, S. Liu, J. Tu, X. Guo, D. Zhang, Modelling of SAW-PDMS acoustofluidics: Physical fields and particle motions influenced by different descriptions of the PDMS domain. *Lab Chip* **19**, 2728–2740 (2019).
67. X. Zhang, Y. Yuan, L. Jiang, J. Zhang, J. Gao, Z. Shen, Y. Zheng, T. Deng, H. Yan, W. Li, W. W. Hou, J. Lu, Y. Shen, H. Dai, W. W. Hu, Z. Zhang, Z. Chen, Endoplasmic reticulum stress induced by tunicamycin and thapsigargin protects against transient ischemic brain injury: Involvement of PARK2-dependent mitophagy. *Autophagy* **10**, 1801–1813 (2014).

Acknowledgments: The authors thank Dr. Liangfei Tian of Zhejiang University for providing DPPC vesicles. **Funding:** This work was supported by National Natural Science Foundation of China (grant nos. 12022410 and 12227809 to L.M., 12104477 to N.R., and 11774371 to L.N.), Chinese Academy of Sciences (YJKYYQ20210019 to L.M.), CAS Key Laboratory of Health Informatics Fund (2011DP173015 to H.Z.), Natural Science Foundation of Guangdong Province (202381515040008 to L.M.), and Shenzhen Basic Science Research (JCYJ20200109110006136 L.M.). This material is based upon work supported by the National Science Foundation Graduate Research Fellowship under grant no. 2139754 (to J.R.). **Author contributions:** X.L. and N.R. designed and performed experiments, analyzed the data, and wrote the manuscript. Z.T., J.R., C.W., L.N., L.M., T.J.H., and H.Z. revised the manuscript. P.L. and L.H. performed numerical simulations. Y.D. performed the MCAO model construction. W.Z. designed the SAW device, and C.W. fabricated the SAW device. P.Z. and Y.C. fabricated and characterized CdTe quantum dots. L.M., T.J.H., and H.Z. supervised the project. All authors edited and approved the final manuscript. **Competing interests:** T.J.H. has cofounded a startup company, Ascent Bio-Nano Technologies Inc., to commercialize technologies involving acoustofluidics and acoustic tweezers. The other authors declare that they have no competing interests. **Data and materials availability:** All data needed to evaluate the conclusions in the paper are present in the paper and/or the Supplementary Materials.

Submitted 7 August 2023
Accepted 19 March 2024
Published 17 April 2024
10.1126/sciadv.adk1855